

Article

Preparation of Porous Biochars by the Co-Pyrolysis of Municipal Sewage Sludge and Hazelnut Shells and the Mechanism of the Nano-Zinc Oxide Composite and Cu(II) Adsorption Kinetics

Xi Chen [†], Ran Zhang [†], Bing Zhao, Guangjian Fan, Haibo Li, Xinyang Xu ^{*} and Mingchuan Zhang

School of Resource and Civil Engineering, Northeastern University, Shenyang 110819, China; chenxineu@mail.neu.edu.cn (X.C.); 1870896@stu.neu.edu.cn (R.Z.); zhaob@mail.neu.edu.cn (B.Z.); 2001057@stu.neu.edu.cn (G.F.); 1901068@stu.neu.edu.cn (H.L.); zhangmingchuan@mail.neu.edu.cn (M.Z.)

^{*} Correspondence: xuxinyang@mail.neu.edu.cn

[†] Xi Chen and Ran Zhang are co-first authors about this work.

Received: 17 August 2020; Accepted: 15 October 2020; Published: 19 October 2020



Abstract: Municipal sewage sludge (MSS) and hazelnut shells were selected for co-pyrolysis and chemically activated with K_2CO_3 in a N_2 atmosphere. The biochar was then modified by photocatalysis. Hazelnut shells, as a solid waste, were selected as a carbon source additive because of its high cellulose content and similar structure to natural wood. Using hazelnut shells could increase the specific surface area, enhance the porosity, and improve the adsorption capacity of the biochar. Hazelnut shells could also reduce the content of heavy metals in the raw biochar materials, along with increasing the ecological security of biochar and contributing to its further development and utilization. FTIR was used to study the changes in the functional groups on the biochar surface. The layered porous structure of the biochar was observed by SEM. The Cu(II) adsorption capacity of the biochar was 42.28 mg/g after 24 h. The Langmuir and pseudo-second-order models effectively described Cu(II) adsorption.

Keywords: co-pyrolysis; alkaline activating agent; Cu(II) adsorption; porous structure; photocatalysis

1. Introduction

In recent years, the number of sewage treatment plants has increased. The construction and operation of a large number of sewage treatment plants enable the effective control of municipal sewage and industrial wastewater. However, a large amount of sludge produced by sewage treatment plants is not properly treated, which causes serious environmental problems [1]. Sludge from sewage treatment plants is rich in microbial organic matter, thereby increasing the number of microbial organisms [2] and pollutants in sewage. It contains a large amount of not only organic-inorganic carbon, nitrogen, phosphorus, potassium and other nutrients but also organic matter, parasite eggs [3], heavy metals [4] and other toxic and harmful substances. The main method of municipal solid waste treatment is separation in the process of waste collection, and the goal is to reuse materials [5]. As an organic-inorganic complex, it can utilize its high content of carbon to carry out an oxygen-free pyrolysis treatment, thereby effectively retaining the carbon in it [6], improving the production rate of biochar, preparing biochar with a high added value, and recycling the mixed combustible gas and other by-products produced in the production process. The process of high temperature dry distillation and pyrolysis of sludge refers to the process method of coal pyrolysis of sludge after drying and drying to produce combustible gas, tar, phenol, acetone, methanol and other chemical raw materials.

Hazelnut shells and sludge were selected for co-pyrolysis. The cellulose and hemicellulose contents in hazelnut shells are higher than those in sawdust, and the lignin content is also higher than

that in sawdust. This property can increase the specific surface area of biochar, enhance the porosity, and improve the adsorption capacity of biochar [7]. As biomass, hazelnut shells are more than 40% cellulose [8]. This cellulose contributes to providing a high specific surface area and optimizes the porous structure of biochar during co-pyrolysis [9]. Compared with hazelnut shells, the regeneration of wood resources is slow, time consuming and relatively expensive [10]. In contrast, hazelnut shells are inexpensive and easy to obtain as a kind of waste [11].

In recent years, pyrolysis and gasification technology has emerged to increase energy output and reduce environmental impact [12]. Pyrolysis technology has been used in industrial production for a long time [13]. It was first used for the carbonization of coal and other materials and was then gradually applied to the petroleum cracking process. A previous study indicated that heavy metals in municipal sewage sludge (MSS) can be transformed from a weakly bound state to a stable state via the pyrolysis process to ensure their security during applications [14]. Pyrolysis technology offers a practical and alternative method for the stabilization and resource utilization of sewage sludge [15]. Sludge pyrolysis technology refers to the thermal decomposition of sludge in an inert atmosphere at atmospheric pressure, which transforms the contained organic matter into hydrocarbons [16]. The final products are tar, pyrolysis gas and carbon [17]. Part of the products can be burned as a heat source for pre-drying and pyrolysis, and the remaining energy can be recovered in the form of oil. Additionally, the biochar produced by pyrolysis can be used as an effective and multipurpose biomass material, for example, as adsorbents [18,19], a potential fertilizer [20], or a feedstock for energy production [21]. Sludge gasification technology refers to the use of air, oxygen or steam as gasification agent to convert organic components in sludge into clean combustible gases containing H_2 , CH_4 , CO and CO_2 . Joan et al. [22] studied the effects of gas residence time and air equivalence ratio on the distribution of sludge gasification products and gas composition by using a bubbling fluidized bed experimental platform. Petersen et al. [23] developed a circulating fluidized bed sludge gasification device, and studied the effects of gasification agent ratio (CO_2/N_2), gasification temperature, material level height and fluidization speed on gasification products. Gross et al. [24], a group of German scholars, proposed ETVS and NTVS processes for the overall treatment and utilization of sludge, with fluidized bed gasification technology as the core, including several units such as sludge dewatering, drying, gasification, combustion and secondary energy generation. High pressure dewatering and solar energy utilization technologies are respectively adopted in sludge dewatering and drying. The two processes can process and transform the wet sludge in different units, and finally output the available electric energy and heat energy. Finally, only residual mineral ash is treated as waste. The economy of the process is evaluated. In addition to meeting its own heat demand, the surplus heat and electricity can be output.

Wet air oxidation technology refers to a chemical process in which pure oxygen or air is used as oxidant at a certain temperature and pressure to make the organic components in the sludge undergo thermal degradation, hydrolysis and oxidation in the aqueous phase, and finally transform into CO , H_2O and N_2 . There are many factors affecting the wet air oxidation process, such as reaction temperature, reaction pressure, reaction time, raw material properties and catalyst use, among which the reaction temperature is the key factor. The whole process of wet oxidation can be realized under two different conditions, one is the subcritical condition lower than $374\text{ }^\circ\text{C}$ and 10 MPa pressure; the other is the supercritical condition higher than $374\text{ }^\circ\text{C}$ and 21.8 MPa .

Biochar is widely used in ecological restoration and agriculture because of its large specific surface area, high stability and strong adsorption capacity. The ability of biochar to absorb pollutants depends on its physical and chemical properties. The properties of biochar produced with different raw materials and under various cracking conditions are quite diverse. Due to the preparation of biochar from the direct pyrolysis of sludge, the specific surface area of the carbon material is not ideal, and the porosity is not sufficiently developed. Therefore, sludge is usually chemically activated before pyrolysis [25]. Okman et al. [26] used grape seed with K_2CO_3 and KOH to produce activated carbon. The sludge-based carbon materials were prepared by a chemically activated pyrolysis. First, the raw

sludge materials were mixed evenly with various chemicals, and then pyrolysis was carried out in an inert atmosphere to obtain biochar with a certain porosity. Through the oxidation and dehydration of chemical activators, hydrogen, oxygen and a small amount of the carbon in raw sludge materials could escape in the form of water vapor and other gases, which formed pores when passing through the carbon layer structure of polycondensated carbon.

Semiconductor photocatalysts have the advantages of a low energy consumption, a lack of secondary pollution, and an ability to convert most organic compounds into carbon dioxide, water and inorganic salt molecules [27]. However, in the actual process, there are the following shortcomings: First, most of the semiconductors have a low utilization of sunlight and second, the photogenerated electron hole pairs of semiconductors easily recombine, which reduces the quantum yield of light, thus affecting the photocatalytic efficiency. In the process of semiconductor photocatalysis, photogenerated electrons and holes are produced by semiconductor materials under the excitation of light, and then an oxidation-reduction reaction occurs with the groups on the surface of the semiconductor to produce active species or intermediate chemical substances that release heat, while the active species or intermediate chemical products with strong oxidation abilities can oxidize and degrade organic pollutants [28]. A large number of studies show that semiconductor photocatalysis technology can not only degrade various organic aromatic compounds in water [29] but also oxidize or decompose toxic precious metal ions in water; these precious metals can be converted into non-toxic or slightly toxic forms to realize the recovery and utilization of precious metals [30]. Photocatalysts used in the photocatalytic degradation of organic wastewater are inexpensive, non-toxic, stable, recyclable, and do not produce secondary pollution; furthermore, some photocatalytic materials can also directly use sunlight. Therefore, semiconductor photocatalysis technology has become an ideal technology for environmental governance. In this experiment, zinc chloride, sodium hydroxide and biochar were used as raw materials to prepare a composite biochar with different proportions of nano-zinc oxide by a hydrothermal synthesis. The composition, structure and morphology of the composite were characterized by X-ray diffraction (XRD), scanning electron microscopy (SEM) and Fourier transform infrared (FTIR) spectroscopy; additionally, Cu(II) adsorption tests were carried out.

In this experiment, SEM, FTIR, XRD and other modern analytical methods were used to characterize the surface features, surface functional groups and internal crystal structure of biochar, respectively, when prepared under different pyrolysis conditions; additionally, the actual adsorption of Cu(II) by biochar and adsorption kinetic models were determined.

2. Materials and Methods

2.1. Raw Materials

The sludge used in this experiment is from the sludge dewatering room of a sewage treatment plant in China. The sludge was dewatered by adding 0.4 wt% polyacrylamide to the non-dewatered sludge and then dewatering it with a screw filter press. The resulting sludge looked similar to black mud. According to the Chinese national standard (Chinese standard method (CJ/T 221-2005)), the moisture content of sludge was approximately 78.55%, the content of organic matter was 65.73%, and the initial pH value was 5.85. It was confirmed that there was a rich content of organic matter in the sludge, and this organic matter could be used as the main raw material for preparing biochar by pyrolysis. The raw materials (sludge and hazelnut shells) were analyzed with the industrial analysis of Chinese coal (Chinese standard method (GB/T 212-2008)) and an element analyzer (Elementar Analysensysteme GmbH (Langensfeld, Germany), vario EL cube V 1.2.1). The proximate and ultimate analyses of the raw materials are shown in Table 1.

Table 1. Proximate and ultimate analyses of raw materials.

Description	MSS (Municipal Sewage Sludge)	Hazelnut Shells
Proximate analysis (wt%)		
Moisture ^a	78.55	8.22
Volatile matter ^b	60.33	76.57
Ash ^b	33.35	1.23
Fixed carbon ^b	1.16	13.98
Low heating value ^b	15.30	27.82
Ultimate analysis (wt%) ^b		
Carbon content	36.88	48.11
Hydrogen content	5.02	2.62
Nitrogen content	5.03	0.52
Sulfur content	1.17	3.07
Oxygen content ^c	52.01	45.73

^a Received basis after the addition of polyacrylamide (0.4%) and dehydration; ^b Dry basis after heating at 105 ± 5 °C for 24 h; ^c Calculated by mass balance.

In this experiment, the contents of Cu, Ni, Pb, Zn, Cr, and Cd in the sludge were determined by inductively coupled plasma atomic emission spectrometry (ICP-AES, LEEMAN, Prodigy XP) based on the Chinese standard method (GB18918-2002), as shown in Table 2.

Table 2. Contents of heavy metals in MSS.

Element	Heavy Metal Element Content (mg/kg)	Threshold Values ^a	
		China pH < 6.5	China pH \geq 6.5
Cu	117.53	800	1500
Ni	77.27	100	200
Zn	666.67	2000	3000
Pb	111.28	300	1000
Cr	61.38	600	1000
Cd	6.30	5	20

^a According to the Chinese standard method (GB18918-2002).

2.2. Preparation of Raw Materials for Co-Pyrolysis

A mixture of MSS and hazelnut shells was soaked for 24 h with different concentrations of K_2CO_3 , a simple alkaline activator. The ratio of raw material to K_2CO_3 solution was 1:1.5 by weight; additionally, to cut back on environmental pollution, the K_2CO_3 solution was recycled and concentrated back to the target value for reuse. After the soaking step, the MSS and hazelnut shells were placed in a drying oven and dried at 105 ± 5 °C for 24 h. The co-pyrolysis of the MSS and hazelnut shells blend was conducted in a vacuum tube furnace (MTI, OTF-1200-x). Figure 1 shows a schematic diagram of the pyrolysis apparatus. According to the experimental design, 20 g of MSS and hazelnut shell samples were added in a certain biomass addition ratio. Then, the sludge and hazelnut shells were mixed fully and evenly placed into a quartz boat. The sample area of the quartz boat was in the center of the quartz tube, and the pyrolysis system was presented in a previous work [31]. First, the vacuum unit was started to exhaust any remaining air in the equipment for 0.5 h, the nitrogen gas flow rate in the co-pyrolysis process was 0.3 L/min, and the temperature ramp rate $\beta = 10$ °C/min was set for increasing to the final pyrolysis temperature. The duration of a maintained temperature was considered the pyrolysis time in the experiment. After naturally cooling to room temperature, a crude sample of biochar was prepared. Next, the sample was sieved to ≤ 1 mm before being pickled with 10% hydrochloric acid and washed with 70 °C deionized water until the washing solution was

neutral, which was used to remove the residue in the biochar. After drying at $105 \pm 5 \text{ }^\circ\text{C}$, the biochar was placed into a sealed bag and then placed into a dryer for future use.

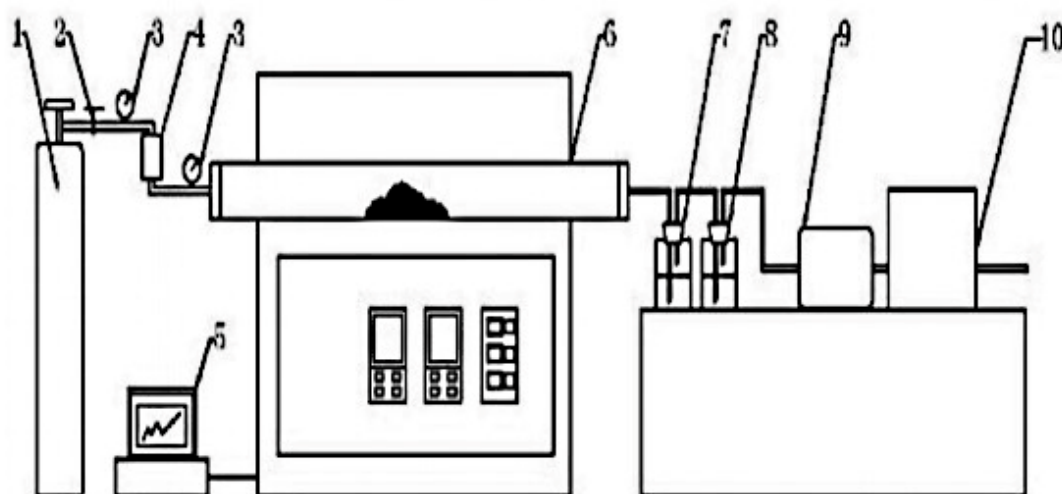


Figure 1. Experimental apparatus for pyrolysis: 1—inert gas (N_2); 2—valve; 3—pressure gauge; 4—flow meter; 5—online temperature monitor; 6—vacuum tube furnace; 7—acid gas washing bottle; 8—alkaline gas washing bottle; 9—active carbon filter; and 10—vacuum pump.

2.3. Preparation of Nano-Zinc Oxide

A total of 3.4073 g of zinc chloride powder was accurately weighed into a conical flask, and then 50 mL of deionized water and 3.0000 g sodium hydroxide was added with stirring. The molar ratio of $\text{OH}^-/\text{Zn}^{2+}$ was 3. After reacting for 30 min, the solution was centrifuged, and then a certain amount of cetyltrimethylammonium bromide (CTAB) was added into a 1:1 alcohol/water solution. Next, the precipitate was added into the alcohol/water solution. The reaction was fully carried out on a magnetic stirrer for 30 min, and then the sample was ultrasonicated for 5 min. Finally, the above solution was transferred to a hydrothermal reactor and sealed. The hydrothermal reaction was carried out at $110 \text{ }^\circ\text{C}$, $120 \text{ }^\circ\text{C}$, $130 \text{ }^\circ\text{C}$, $140 \text{ }^\circ\text{C}$ and $150 \text{ }^\circ\text{C}$ for several hours. The precipitate was washed off with deionized water and alcohol and dried at $80 \text{ }^\circ\text{C}$.

2.4. Preparation of the Biochar/Nano-Zinc Oxide Composite

Zinc chloride powder (3.4073 g) was accurately weighed and placed in a conical flask. Then, 50 mL of deionized water, 3.0000 g sodium hydroxide and a certain amount of biochar (0.5000 g, 1.0000 g, 1.5000 g, 2.0000 g and 2.5000 g,) was added with stirring. The reaction time was 30 min. Next, the solution was centrifuged, and 0.3200 g CTAB was added into 60 mL of a 1:1 alcohol/water solution before adding the precipitate from the centrifuge tube. The reaction was performed to completion on a magnetic stirrer for 30 min, and then ultrasonication was applied for 5 min. Finally, the above solution was transferred to a hydrothermal reactor and sealed. The hydrothermal reaction was conducted at a specific temperature for 20 h. The precipitate was washed with deionized water and alcohol and then dried at $80 \text{ }^\circ\text{C}$ to obtain a sample of the biochar/nano-zinc oxide composite material that was ground and sieved. The single-factor experimental conditions for the preparation of the nano-zinc oxide composite biochar are shown in Table 3.

Table 3. Labeled process variables for the production of various nano-zinc oxide/biochar materials.

Type of Nano-Zinc Oxide			Type of Nano-Zinc Oxide/Biochar		
Preparation temperature of nano-zinc oxide (°C)	110	N110	Amount of added biochar (g)	0.5	G0.5
	120	N120		1.0	G1.0
	130	N130		1.5	G1.5
	140	N140		2.0	G2.0
	150	N150		2.5	G2.5

2.5. Physico-Chemical Properties of the Prepared Biochar

2.5.1. Biochar Yield

Due to the loss of water and the decomposition of organic matter in the process of preparing biochar from MSS and hazelnut shells, different pyrolysis conditions, such as the final temperature, pyrolysis time, activator concentration and ratio of biomass addition, all affected the resulting biochar. To investigate the production of biochar, the biochar yield was calculated with the following equation:

$$\text{Yield of biochar (wt\%)} = \frac{W_{\text{bio-char}}}{W_{\text{raw materials}}} \times 100\% \quad (1)$$

where $W_{\text{bio-char}}$ and $W_{\text{raw materials}}$ are the weights of the biochar and raw materials, respectively. The yield was based on the dry basis weight of the raw materials to evaluate the weight loss of thermal decomposition after co-pyrolysis.

2.5.2. Iodine Absorption Number

The iodine adsorption value is the most commonly used index to characterize the adsorption performance of biochar, and this value can simply and quickly characterize the degree of development of micropores larger than 1.0 nm along with the specific surface area of the biochar. The determination method of the iodine adsorption value in this experiment is based on the determination of the iodine adsorption value in the Chinese national standard (GB/T12496-2015). After acidification, a certain amount of sample was fully vibrated and adsorbed with iodine solution. After filtration, the filter solution was taken, and the residual iodine in the filtrate was titrated with sodium thiosulfate solution. The amount of iodine adsorbed per gram of biochar at a residual iodine concentration of 0.02 mol/L was determined as the iodine value. The test steps are shown in Table 4. The iodine absorption number was calculated by the following:

$$A = \frac{5 \times 10(C_1 - 1.2C_2V_2) \times 127}{M} \times D \quad (2)$$

where A is the iodine number (mg/g), C_1 is the concentration of the iodine solution (mol/L), C_2 is the concentration of sodium thiosulfate (mol/L), V_2 is the titration reading (mL), M is the adsorbent mass (g), and D is the correction factor.

Table 4. Test steps for the determination of the iodine absorption number.

Test Step	Procedure
1	Approximately 0.2–0.5 g of biochar was mixed with 10 mL of HCl (5 wt%) and heated at a low temperature for approximately 30 s
2	Samples were cooled down to room temperature and then shaken with 50 mL of 0.1 mol/L iodine solution for 15 min
3	The dilute filtrate was titrated with 0.1 mol/L sodium thiosulfate until the solution turned pale yellow
4	2 mL of a 1% starch indicator solution was added and titrated until the solution was colorless

2.5.3. Surface Functional Groups

An infrared spectrum analysis is based on the characteristic vibrations of materials to identify the types of skeleton atoms and the changes in surface functional groups and other structural information. This analysis can also be used as a method to characterize and identify chemical species. An infrared spectrum analysis has the following beneficial characteristics, a discriminating characterization of molecular structure, a low energy consumption, an absence of sample damage and a fast analysis. In this experiment, FTIR spectroscopy was used to characterize the functional groups on the surface of biochar. The sample powder was mixed with spectrally pure KBr (mass ratio was approximately 1:99). This mixture was ground into micron-sized powder particles in an agate bowl. Next, the powder was pressed and placed in the optical path. The spectral scanning range was 4000–400/cm, and the resolution was 4/cm.

2.5.4. Crystal Structure

The principle of XRD is that the X-ray passes through a crystal, which acts as a grating, and a large number of particles (atoms, molecules and ions) produce coherent scattering and light interference; thus, the intensity of the scattered X-ray increases and decreases. The crystal surface spacing is calculated by the Bragg formula for structural analysis. An XRD analysis was used to identify the changes in the crystal structure of the biochar samples prepared under different conditions. The samples were ground to 75 μm , and a Cu K α radiation source was used in a scanning range of 5–80 $^{\circ}\text{C}$.

2.5.5. Micromorphology

The micromorphology of the samples was observed by SEM (ZEISS Ultra Plus, OXFORD X-Max 50 mm² (S/N:52519)). Electron scanning is based on a fine focused electron beam scanning the surface of the sample to generate a secondary electronic signal. After amplification, the surface morphology of the sample is generated as an image on a cathode-ray tube. SEM can be used to analyze the micromorphology, micro-structure and interfacial state of materials. Furthermore, SEM can directly image the porosity, pore size and morphological characteristics of materials. A three-dimensional image of the sample can be obtained by SEM, which makes it widely used for analyzing the structure and morphology of porous materials. In this experiment, SEM was used to observe, compare and analyze the MSS and biochar samples prepared under different conditions. In the pre-treatment, the samples needed to be sprayed with gold to increase their conductivity.

2.5.6. Adsorption Experiments

Carbon material, as an adsorbent, is very efficient for removing heavy metals from aqueous solution. However, due to the different types of biochar and experimental conditions, the description of the adsorption process and the adsorption mechanism of heavy metal adsorbates are also different. To explore the actual adsorption capacity of biochar samples, Cu(II) was selected as the adsorbate, and CuSO₄·5H₂O was used to prepare a Cu(II) solution. Briefly, 0.01 mol/L Na₂SO₄ was used as

the supporting electrolyte, along with a certain amount of biochar and the addition of 50 mL of Cu(II) solution at a certain mass concentration. Then, the pH of this mixture was adjusted to a specified value with a dilute H₂SO₄ or NaOH solution. The sample was shaken at a rate of 150 r/min at room temperature (25 °C). The supernatant was collected after filtration and the concentration of Cu(II) in the supernatant was determined by ICP-AES. The adsorption capacity of the biochar was calculated according to Equation (3):

$$Q_e = \frac{(C_o - C_e)V}{M} \quad (3)$$

where Q_e (mg/g) is the adsorption quantity; C_o (mg/L) and C_e (mg/L) are the initial and equilibrium concentrations, respectively; V (L) is the volume of the solution; and M (g) is the mass of the biochar.

3. Results and Discussion

3.1. Yield and Iodine Adsorption Number of the Prepared Biochar

Under the following conditions, a pyrolysis time of 1 h, a K₂CO₃ concentration of 4 mol/L and a biomass addition of 30%, the effects of the final pyrolysis temperature as a single-factor variable were discussed in terms of biochar yield and the iodine adsorption value. After activation by K₂CO₃, the yield of biochar decreases with an increasing final pyrolysis temperature (Figure 2a). Due to the gradual decomposition of the organic and inorganic components, the yield of biochar is 61.03% at the final pyrolysis temperature of 500 °C. At the final pyrolysis temperature of 850 °C, the yield of biochar decreases to 37.76%, the weight loss is 62.24%, and the iodine adsorption value of the biochar reaches the maximum value, which indicates that the activation temperature of K₂CO₃ is 850 °C for the co-pyrolysis of MSS and hazelnut shells. This result is similar to previous studies [32]. In terms of the iodine adsorption value, this value for the biochar activated by K₂CO₃ shows a single upward trend, especially at the final pyrolysis temperature of 750 °C, where the iodine adsorption value increases rapidly, and reaches 812.01 mg/g at 850 °C. At a high temperature, K₂CO₃ molecules are impregnated into the raw material. Then, the organic and inorganic carbon are carbonized and deposited on the carbon skeleton. Finally, after the residue is washed with acid and deionized water, a porous biochar with a very large surface is formed; and the stronger the activation of K₂CO₃ is, the stronger the adsorption performance of the biochar.

With increasing pyrolysis time, as shown in Figure 2b, the yield of biochar decreases gradually and shows a single decreasing trend. It can be seen that with the increase in the final pyrolysis temperature and pyrolysis time, the organic and inorganic substances in the MSS and hazelnut shells gradually undergo a thermal decomposition reaction, which transforms them into gaseous and liquid products; thus, the amount of solid products gradually decreases. When the pyrolysis time is increased from 15 to 120 min, the yield of biochar decreases from 65.25 to 52.73%, and the weight loss is 12.52%. As the final pyrolysis temperature is higher, the degree of decomposition of the organic and inorganic components is higher. With increasing pyrolysis time, the degree of weight loss decreases. At the final pyrolysis temperature of 850 °C, the pyrolysis time increases from 15 to 90 min, the yield of biochar decreases from 40.67 to 30.17%, and the weight loss is 10.5%. With increasing pyrolysis time, the iodine adsorption value of biochar presents a single peak form. Under the condition of a 45 min pyrolysis time, the iodine adsorption value reaches 1065.25 mg/g, indicating that the K₂CO₃ activator has an obvious activation effect on the raw materials (MSS and hazelnut shells) and that a porous biochar structure is developed. In terms of the iodine adsorption value of biochar, the iodine adsorption value first increases and then decreases with an increasing final pyrolysis temperature and pyrolysis time. It can be seen that the pyrolysis process has a suitable range for the final temperature and pyrolysis time parameters. With increasing final temperature and pyrolysis time, the activator molecules react with the hazelnut shells and MSS and then gradually etch a porous structure on its surface. At the initial stage, small micropores are formed with large specific surface areas, which is conducive to adsorption. With the further increase in both the final temperature and pyrolysis time, the etching reaction increases

continuously. The existing pores expand and collapse under the action of long-term activation, which further etches the initial micropores into mesopores. If the time is too long, a portion of the pores will be sintered, and the sintering may destroy the pore wall between the adjacent pores in biochar, thereby leading to the collapse of the framework. The number of micropores will not increase, while some micropores and mesopores will be destroyed and transformed into mesopores and macropores. Thus, the specific surface area will gradually decrease, the degree of porosity will gradually decrease, and then the adsorption capacity of the biochar will decrease.

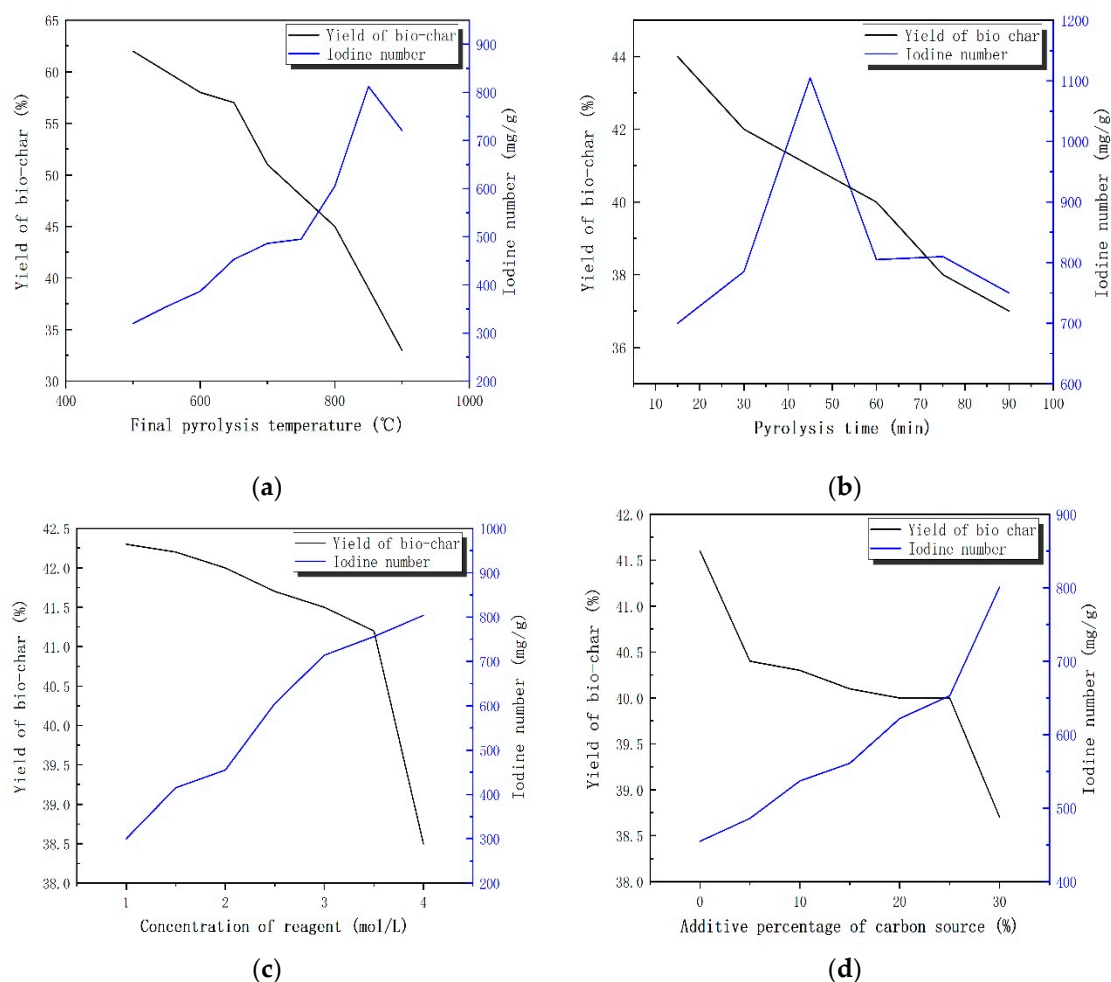
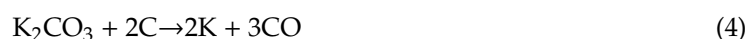


Figure 2. The yield and iodine adsorption number of the biochar samples under different process variables: (a) Final pyrolysis temperature; (b) Pyrolysis time; (c) Concentration of reagent; (d) Percentage of added carbon source.

When the pyrolysis temperature and time are fixed, the production of biochar fluctuates less. The iodine adsorption value of biochar increases with increasing K_2CO_3 concentration (Figure 2c). When the concentration of K_2CO_3 is increased from 1 mol/L to 4 mol/L, the iodine adsorption value of biochar increases from 273.71 mg/g to 763.01 mg/g, indicating that the activation effect of K_2CO_3 is significant. The activation mechanism of K_2CO_3 is that it reacts with carbon atoms on the surface of the raw materials in an inert atmosphere to form K and CO, and the reaction is shown in Equation (4) [33]:



When the ratio of added biomass increases, as shown in Figure 2d, the yield of biochar decreases. The volatiles of the MSS and biomass are released gradually in the pyrolysis process. As the volatiles of the hazelnut shells are higher than those of the MSS itself, the increase in the ratio of added hazelnut

shells decreases the biochar yield. However, the addition of hazelnut shells significantly contributes to the adsorption properties of biochar. When the ratio of added biomass increases, the specific surface area of biochar and the adsorption capacity of iodine are greatly improved. Hazelnut shells contain more cellulose and hemicellulose, which is similar to the raw materials of commercial activated carbon. Therefore, adding hazelnut shells is beneficial to the function of biochar.

3.2. FTIR Spectroscopy and XRD Results for the Biochar

The previous work of our group carried out detailed FTIR and XRD analyses on biochar without a photocatalyst modification [34]. In this paper, FTIR and XRD analyses of biochar modified by photocatalysts are mainly carried out. Figure 3 shows the FTIR spectrum of the photocatalyst-modified biochar.

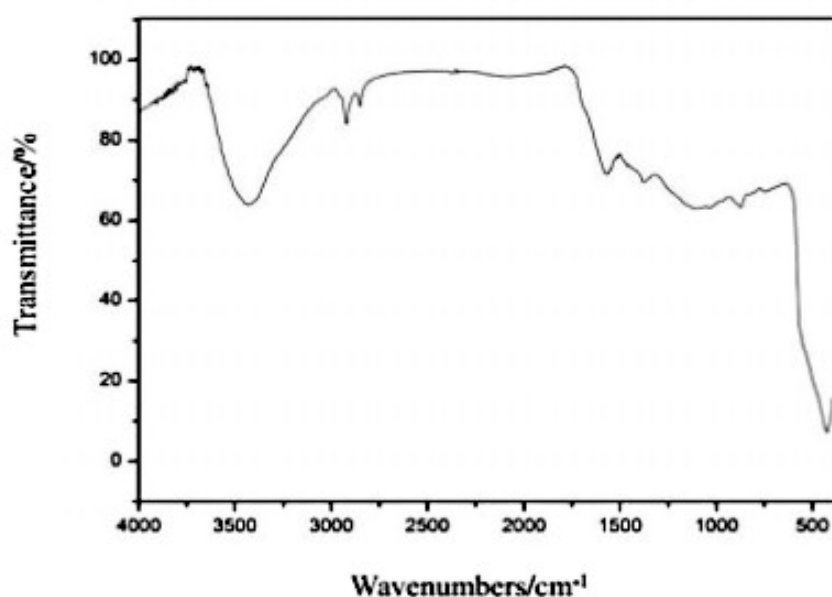


Figure 3. FTIR spectra of the photocatalyst-modified biochar.

Figure 3 shows that the peak near 427 cm^{-1} is the characteristic ZnO peak. There is a wide absorption peak near 1030 cm^{-1} , which is the absorption vibration peak of the C-C bond. The absorption peaks at 1569 cm^{-1} , 873 cm^{-1} , 813 cm^{-1} and 748 cm^{-1} are similar to those in the bamboo charcoal spectrum, indicating that the surface structure of the biochar in the composite did not change. The absorption peaks of KBr near 1380 cm^{-1} , 2850 cm^{-1} and 2920 cm^{-1} are the absorption peaks of the organic matter in CTAB, indicating that there are some impurities remaining after the washing process. The absorption peaks near 3430 cm^{-1} and 1630 cm^{-1} are the absorption peaks of light radicals adsorbed on the surface of the sample and water molecules in the air.

Figure 4 shows the XRD pattern of nano-zinc oxide-modified biochar. It can be seen from Figure 4 that there are diffraction peaks corresponding to the (100), (002), (101), (102), (110), (103), (200), (112) and (201) crystal planes of zinc oxide crystals, indicating that the zinc oxide in the biochar/nano-zinc oxide composite has a hexagonal wurtzite structure. The diffraction peaks are sharp, which confirms good crystallization, and the peak positions do not change, which indicates that the structure and crystal form of nano-zinc oxide does not change. It can also be seen that the 2θ angle is 23° . There are symmetrical diffuse diffraction peaks near the amorphous structure of biochar, which are originally at a 2θ angle of 43.5° . There is a weak peak in the vicinity, but it is difficult to observe. This peak corresponds to the diffraction peak of the (004) crystal plane. This weak peak may be the result of the growth of graphite-like microcrystals in the biochar; thus, the carbon network plane increases significantly in the two-dimensional direction.

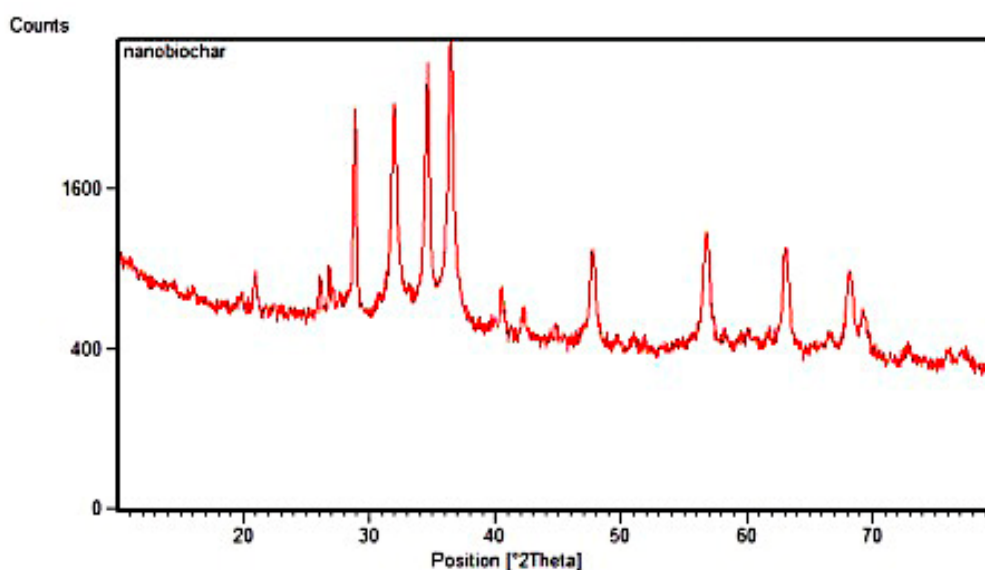


Figure 4. XRD pattern of the nano-zinc oxide-modified biochar.

3.3. Micro-Morphology

The biochar samples were washed, pickled, dried, and ground through a 200 mesh screen; then, the surfaces of the dried MSS and biochar samples were magnified 2000–20,000 times by SEM for observation and analysis. Figure 5a shows the surface morphology of the dried MSS without pyrolysis. Figure 5b shows the surface morphology of the biochar sample before activation. Figure 5c shows the surface morphology of the biochar without the photocatalyst modification, and Figure 5d shows the surface morphology of the biochar modified by the photocatalyst.

Figure 5a shows the surface morphology characteristics of the dry MSS without pyrolysis. After being magnified 5000 and 20,000 times, it can be seen that the surface of the dried sludge is flat without any depressions or pores. When the MSS and hazelnut shell samples are pyrolyzed at 500 °C for 1.5 h without activation (Figure 5b), the surface of the biochar products become sintered showing uneven and slightly nucleated characteristics.

Figure 5c shows the surface morphology of the biochar after the co-pyrolysis of the MSS and hazelnut shell samples at 850 °C for 1 h after being activated by 4 mol/L K_2CO_3 . The nano-pore structure of the biochar surface is extremely evident and is characterized by a decrease in the pore diameter, an increase in the pore density and an increase in the specific surface area.

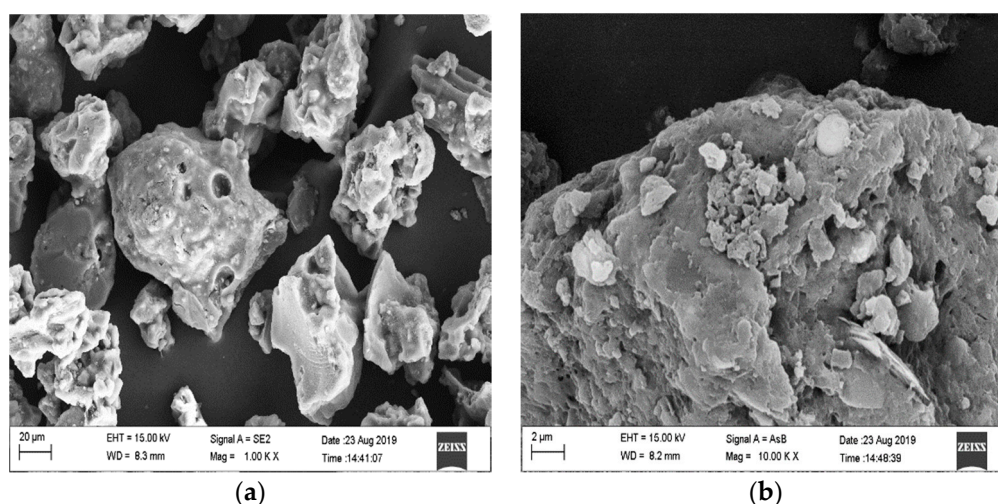


Figure 5. Cont.

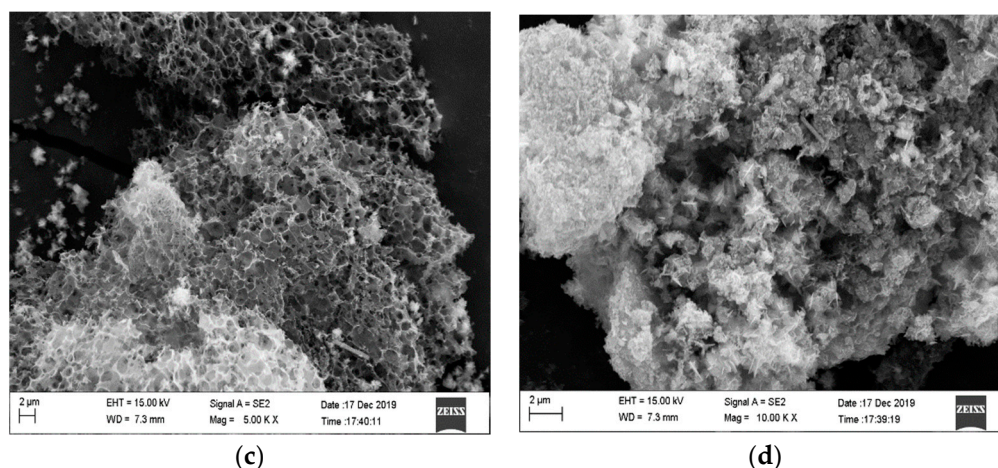


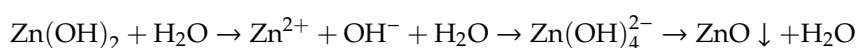
Figure 5. SEM micrographs of MSS (a); The surface morphology of the biochar sample before activation (b); The surface morphology of biochar without the photocatalyst modification (c); and the surface morphology of the biochar modified by the photocatalyst (d).

Figure 5d shows the SEM images of the nano-zinc oxide/biochar composites at different magnifications. The zinc oxide image shown in Figure 5d shows that the product has a uniform particle size and good dispersion. These zinc oxide nanoparticles are composed of uniform, small and ordered nanosheets that seem to follow certain rules, with a diameter of approximately 500 nm and a thickness of approximately 15 nm. They are interlaced to form a three-dimensional flower-like layered structure with a diameter of approximately 2 μm .

The functional mechanism of the K_2CO_3 activator lies in two points: one is that K_2CO_3 reacts with C to generate CO gas, and a large amount of CO is released from the MSS and hazelnut shells, leaving paths through the material that contribute to the nano-porous structure of the biochar materials and significantly increase the specific surface area; the other is that the reaction between the MSS and hazelnut shell activators K_2CO_3 and C directly causes surface cavities, which appear after being at the final pyrolysis temperature. Additionally, with the further increase in pyrolysis time, the porosity gradually increases. Thus, both of the above contribute to the increased specific surface area of the biochar, resulting in a significant increase in the adsorption capacity of the biochar. When the final pyrolysis temperature is 850 $^\circ\text{C}$, the pyrolysis time is 1 h, and the concentration of K_2CO_3 is 4 mol/L, the concentration of the activator is large and the degree of activation is high; thus, the surface of the biochar slightly expands, a small amount of the pore structure sinks and collapses, and the whole biochar resembles a honeycomb structure.

3.4. Study on the Growth Mechanism of Nano-Zinc Oxide

The morphology and size of nanocrystals are determined by the internal structure of the crystal and are also affected by external conditions. To obtain nanorods, it is necessary for the nanoparticles to undergo anisotropic growth. Under hydrothermal conditions, the growth process of zinc oxide nanorods is first accomplished by the hydrolysis of a $\text{Zn}(\text{OH})_2$ colloid under alkaline conditions, and then the growth unit $\text{Zn}(\text{OH})_4^{2-}$ is formed by the oxygen bridge between the growth units and the protonation reaction of anion groups. Next, the growth unit continues to grow on the crystal nucleus, resulting in the formation of nanorods. Equation (5) shows the reaction:



Due to the introduction of CTAB as a surfactant in this experiment, its presence will inevitably reduce the interfacial surface energy, which is conducive to the formation of a new phase in the solution,

that is, the formation of a crystal nucleus. CTAB is a cationic surfactant that completely dissociates in water to form cationic $C_{19}H_{42}N^+$ with hydrophobic groups. Furthermore, CTAB can form ion pairs with $Zn(OH)_4^{2-}$ through electrostatic attraction, as shown in Figure 6. Thus, CTAB plays a role in transporting growth units. At the same time, the CTAB surfactant can also be adsorbed on the crystal surface of zinc oxide nanocrystals during the growth of zinc oxide nanorods as well as forming an ordered hydrophobic film. When the CTAB surfactant transports the growth unit to grow on the crystal nucleus, there is anisotropic growth that occurs due to the existence of a hydrophobic film. The surface-to-surface bonding (Figure 6c) on the [0001] plane is absolutely dominant, and the growth model is shown in Route 1 in Figure 6b. When the growth unit needs to grow in the radial direction of the nanorods, the growth units are grown by a vertex and edge combination (Figure 6d). Due to the existence of an ordered hydrophobic film on the surface of the nanocrystals, it is difficult for the growth units to reach the surface of the crystal, and the growth in this direction is limited (Figure 6, Route 2). These factors lead to the generation of nanorods with small diameters. At the same time, an ethanol/water system with low interfacial tension is used in this experiment. Compared with pure water, the ethanol/water system can effectively reduce the surface tension of the solution, energy required for the formation of zinc oxide nanocrystals, and nucleation and growth rate of zinc oxide nanocrystals, all of which are conducive to the formation of zinc oxide nanorods with small diameters and large aspect ratios.

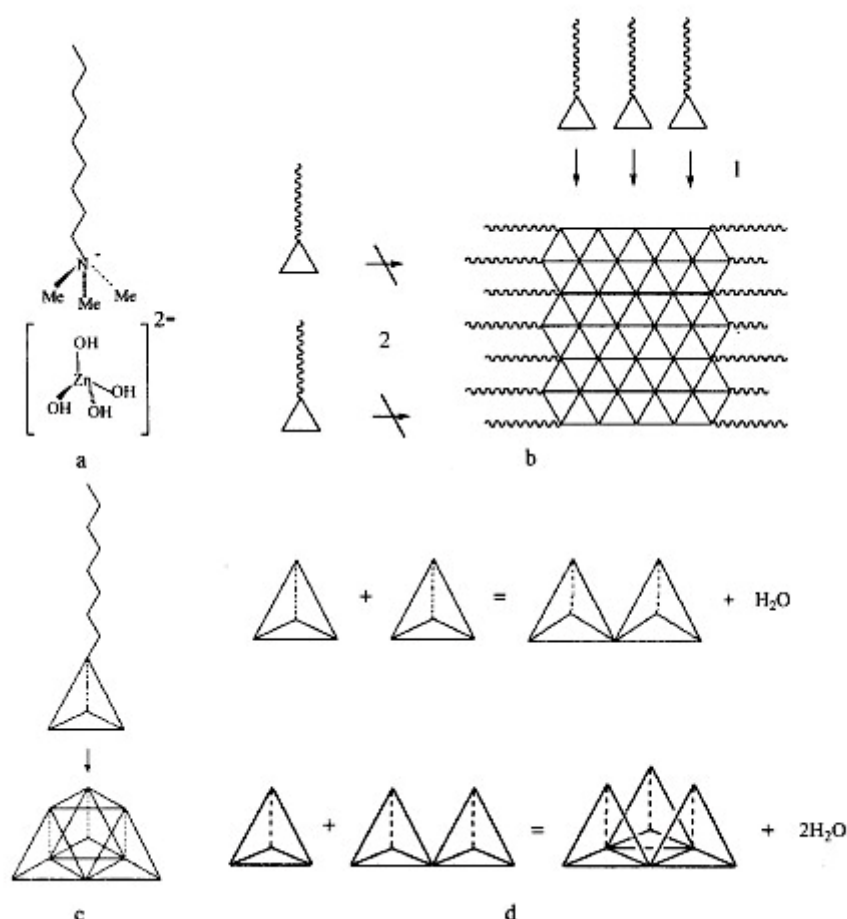


Figure 6. Diagram of CTAB promotion in the growth of nano-zinc oxide. (a): An ion pair formed by electrostatic attraction; (b): Growth model of nano-zinc oxide; (c): Growth forms of nano-zinc oxide; (d): Growth model of nano-zinc oxide).

3.5. Isothermal Adsorption Model and Kinetic Model of Cu(II) by the Biochar

K₂CO₃-modified biochar with good specific surface area and porosity was selected. The pyrolysis conditions were as follows: final pyrolysis temperature of 850 °C, pyrolysis time of 1 h, 4 mol/L K₂CO₃ activator, and a 30% addition of hazelnut shells. After cleaning, the biochar was dried and ground through a 200 mesh sieve at a dose of 1.25 g/L.

3.5.1. Cu(II) Adsorption Experiment

In the isothermal adsorption experiment, the initial concentration of Cu(II) solution was C₀ = 0, 20, 40, 50, 60, 75, 80, and 100 mg/L. The biochar and Cu(II) solution were encapsulated in a conical flask and shaken at 110 rpm for 24 h at room temperature (25 °C). Next, a 0.45 µm filter membrane was used to separate the biochar and Cu(II) solution, and the concentration of Cu(II) in the solution was determined by ICP. Table 5 shows the Cu(II) adsorption capacity of the biochar.

Table 5. Adsorption capacity of Cu(II) on the biochar.

C _e (mg/L)	3.25	5.26	8.37	12.58	25.62	30.16	45.56
C ₀ (mg/L)	20	40	50	60	75	80	100
Q _e (mg/g)	16.85	30.73	35.62	40.25	41.37	41.62	42.28

Table 5 shows that with the increase in the initial concentration of Cu(II), the adsorption capacity of the biochar increases rapidly, indicating that under the condition of a low concentration of adsorbate, the initial concentration of Cu(II) has a great influence on the adsorption capacity of the biochar. When the initial concentration of Cu(II) is 60 mg/L, the adsorption capacity of the biochar is 40.25 mg/g, and the adsorption capacity tends to be slightly increased with increasing initial concentration. When the initial concentration of Cu(II) is 100 mg/L, the adsorption capacity of the biochar reaches the maximum value, approximately 42.28 mg/g. According to the IUPAC classification [35], the N₂ adsorption-desorption isotherm of the biochar is similar to the type IV isotherm and type H2 hysteresis loop.

The Langmuir and Freundlich models were used to describe the adsorption isotherm of the biochar to Cu(II). The Langmuir model mainly describes the adsorption process of a single molecular layer [36]. This model assumes that the surface properties of the adsorbents are the same, and each surface molecule or atom with a residual valence force adsorbs a gas molecule; thus, gas molecules adsorb on the solid surface as a single layer. Furthermore, the adsorption is dynamic, and the adsorbed molecule can return to the gas phase under the influence of heat; thus, the adsorption process is similar to the condensation process of a gas, and the desorption process is similar to the evaporation of a liquid. When the adsorption equilibrium is reached, the adsorption speed is equal to the desorption speed; the condensation speed of gas molecules on the solid surface is directly proportional to the partial pressure of each component in the gas phase; additionally, there is no force between the gas molecules adsorbed on the solid surface. The Freundlich model is an empirical equation without any hypothesis. It is generally believed that the value of 1/n is between 0 and 1. The value of 1/n indicates the strength of the influence of concentration on the adsorption capacity [37]. The smaller 1/n is, the better the adsorption performance.

Equation (6) shows the Langmuir adsorption isotherm:

$$\text{Langmuir isotherm : } \frac{C_e}{Q_e} = \frac{1}{K_L Q_m} + \frac{C_e}{Q_m} \quad (6)$$

where C_e (mg/L) is the equilibrium concentration of the adsorbate, Q_e (mg/g) is the adsorption quantity at equilibrium, Q_m (mg/g) is the theoretical maximum monolayer adsorption capacity of the adsorbate, and K_L (L/mg) is the Langmuir isotherm coefficient.

Equation (7) shows the Freundlich adsorption isotherm:

$$\text{Freundlich isotherm : } \ln Q_e = \ln k_F + \frac{\ln C_e}{n} \quad (7)$$

where k_F (L/mg) is the Freundlich isotherm coefficient and n is the Freundlich adsorption constant.

By plotting C_e/Q_e versus C_e and $\ln Q_e$ versus $\ln C_e$, we can calculate Q_m , K_L , k_F and n . Table 6 shows the results.

Table 6. Fitting parameters of the Langmuir and Freundlich adsorption isotherms.

Langmuir Isotherm Model		Freundlich Isotherm Model	
Q_m (mg/g)	43.54	K_F (L/mg)	19.29
K_L (L/mg)	0.62	n	4.19
R^2	0.99963	R^2	0.77546

According to Table 6, the fitting correlation coefficient R^2 of the Langmuir model is larger than that of the Freundlich model and is more than 0.99. Therefore, it is confirmed that the Langmuir adsorption isotherm can better characterize the adsorption characteristics of the biochar to Cu(II). The biochar material prepared by the co-pyrolysis of MSS and hazelnut shells demonstrates monolayer adsorption for Cu(II). The values of n in Table 6, which are between 1 and 10, indicate the heterogeneity of the adsorbents [38]. Theoretically, the maximum adsorption capacity of the biochar for Cu(II) is 43.54 mg/g. This good fit with the Langmuir model is in good agreement with the studies of other authors [39]. In the adsorption experiment, when the initial concentration of Cu(II) is 100 mg/L, the adsorption capacity of biochar is 42.28 mg/g, which is close to the maximum adsorption capacity and shows that the adsorption process is basically completed within 24 h and that the adsorption capacity is close to saturation.

3.5.2. Isotherm Adsorption Model and Kinetic Model of Cu(II)

In the model experiment of adsorption kinetics, the initial concentration of Cu(II) was 55 mg/L. The biochar and Cu(II) solution were placed in a conical flask and shaken at room temperature (25 °C) for 0 min, 10 min, 30 min, 1 h, 2 h, 5 h, 10 h and 24 h at a rate of 110 rpm. Next, the biochar was separated into the Cu(II) solution by a 0.45 μm filter membrane, and the concentration of Cu(II) in the solution was determined by ICP-AES. Table 7 shows the effect of adsorption time on the adsorption capacity of the biochar.

Table 7. Effect of adsorption time on the adsorption capacity of the biochar.

Time (h)	1/6	0.5	1	2	5	10	24
Q_t (mg/g)	33.37	35.68	37.56	38.12	38.67	40.35	40.60

Table 7 shows that when the concentration of Cu(II) is 55 mg/L and the adsorption time is 1 h, the adsorption capacity of the biochar rapidly increases to 37.56 mg/g, which is due to the existence of a large number of empty active sites on the surface of the biochar. These results are similar to those of biochar derived from other agricultural residues [40]. Additionally, the adsorption capacity of the biochar is 38.12 mg/g after 2 h and has a stable trend. With the increase in adsorption time from 2 to 24 h, the rate of increase in the adsorption capacity gradually decreases. After 24 h of adsorption, the adsorption capacity of the biochar reaches 40.60 mg/g, which is close to the maximum single-layer adsorption capacity obtained from the Langmuir adsorption isotherm.

After much research and deliberation, a model of the adsorption mass transfer rate was proposed [41]. According to the quasi-first-order kinetic model, the rate of metal ions occupying the adsorption sites on the adsorbent surface is positively correlated with the number of unoccupied

adsorption sites on the adsorbent surface, and the quasi-second-order kinetic model is positively correlated with the square of unoccupied adsorption sites on the adsorbent surface. In this experiment, the quasi-first-order and second-order kinetic models were used to fit the kinetic process of Cu(II) adsorption by biochar. The two equations are expressed as follows:

Pseudo-first-order model:

$$\text{Lg}(Q_e - Q_t) = \text{Lg}Q_e - \frac{k_1}{2.303}t \quad (8)$$

Pseudo-second-order model:

$$\frac{t}{Q_t} = \frac{1}{k_2Q_e^2} + \frac{t}{Q_e} \quad (9)$$

where Q_e (mg/g) is the adsorption quantity at equilibrium, Q_t (mg/g) is the adsorption quantity at time t (h), and k_1 (1/h) and k_2 (mg/g h) are the equilibrium rate constants of the pseudo-first-order and pseudo-second-order adsorption, respectively.

By plotting $\text{lg}(Q_e - Q_t)$ versus t and t/Q_t versus t , the adsorption rates k_1 and k_2 can be calculated, and the equilibrium adsorption capacity Q_e (mg/g) can be obtained by using the quasi-first-order and quasi-second-order kinetic models. According to the correlation coefficient of the fitting process of these two kinetic models, it can be concluded that the adsorption kinetic process of Cu(II) to the biochar sample conforms to the quasi-second-order kinetic model. When the adsorption reaches equilibrium, the adsorption capacity of Cu(II) on the biochar is 40.75 mg/g in the quasi-second-order kinetic model, and after 24 h of adsorption, the actual adsorption capacity of the biochar is 40.60 mg/g. Similar results have been reported for Cu(II) adsorption by the biochar produced from *Spartina alterniflora* [42].

As confirmed by the Langmuir model, the adsorption of Cu(II) on the biochar is monolayer adsorption, which belongs to the category of chemical adsorption. The adsorption of the adsorbate by chemical functional groups on the surface of the biochar is the main factor limiting the adsorption capacity. For the biochar adsorbents, the specific surface area, porosity, pore volume and other micro-characteristics comprehensively affect the adsorption capacity. In addition, the surface functional groups also play the role of adsorbate binding sites, and the adsorption mechanism is more complex.

The FTIR spectrum of the biochar also confirms that the surface of the biochar prepared by the co-pyrolysis of MSS and hazelnut shells has oxygen-containing functional groups, such as alcohol hydroxyl groups, phenol hydroxyl groups, carboxylic acids, ethers, and esters. These functional groups, which are provided by the MSS and hazelnut shells, easily combine with the adsorbate and provide considerable adsorption capacity for the biochar. This study provides a theoretical basis for the subsequent development of biochar in the field of adsorbents, especially in the application of pollutant adsorption in water and for improved soil properties.

4. Conclusions

A high temperature and long pyrolysis time decreased the iodine absorption number of biochar because of the further etching effect. The pyrolysis temperature led to important changes in the functional groups, and the biochar underwent graphitization above 850 °C. The biochar material prepared by the co-pyrolysis of MSS and hazelnut shells had a significant specific surface area, porosity and functional group structure. The introduction of biochar did not change the crystal structure of the nano-zinc oxide. The adsorption of Cu(II) by biochar belonged to the Langmuir adsorption isotherm, which is monolayer chemical adsorption, and the composite followed the quasi-second-order kinetic model for the adsorption kinetic process. The co-pyrolysis of sludge and biomass from municipal wastewater treatment plant can not only produce biochar with low-cost and mass production, but also avoid the shortage of using traditional raw materials to prepare biochar, which needs a lot of natural vegetation. Biochar prepared from sludge can be used as adsorbent because of its good pore structure. Moreover, biochar retains nutrients such as carbon, nitrogen, phosphorus and potassium, and immobilizes heavy metals and other pollutants. It can be used as soil conditioner to return to the soil and realize economic value. In addition, the byproducts such as mixed combustible gas and

liquid tar can be recycled as biofuels. In this experiment, biochar and nano-zinc oxide were used to make biochar and have the photocatalytic ability on the basis of its original basic functions. This is of great significance for the treatment of organic wastewater by biochar and promotes research on the multi-functions of biochar.

Author Contributions: Methodology, B.Z.; Project administration, H.L. and X.X.; Resources, M.Z.; Software, G.F.; Writing—review & editing, X.C. and R.Z. All authors have read and agreed to the published version of the manuscript.

Funding: This work was supported by the National Key Research and Development Projects (ZX20200121) and the Fundamental Research Funds for the Central Universities (N180112012).

Acknowledgments: We would also like to thank Chen Qian (Tsinghua University and National University of Singapore).

Conflicts of Interest: The authors declare no conflict of interest.

References

1. Bondarczuk, K.; Markowicz, A.; Piotrowska-Seget, Z. The urgent need for risk assessment on the antibiotic resistance spread via sewage sludge land application. *Environ. Int.* **2016**, *87*, 49–55. [[CrossRef](#)] [[PubMed](#)]
2. Fernando, N.L.; Fedorak, P.M. Changes at an activated sludge sewage treatment plant alter the numbers of airborne aerobic microorganisms. *Water Res.* **2005**, *39*, 4597–4608. [[CrossRef](#)]
3. Fyttili, D.; Zabaniotou, A. Utilization of sewage sludge in EU application of old and new methods—A review. *Renew. Sustain. Energy Rev.* **2008**, *12*, 116–140. [[CrossRef](#)]
4. Fang, W.; Wei, Y.; Liu, J. Comparative characterization of sewage sludge compost and soil: Heavy metal leaching characteristics. *J. Hazard. Mater.* **2016**, *310*, 1–10. [[CrossRef](#)]
5. Panepinto, D.; Genon, G. Carbon dioxide balance and cost analysis for different solid waste management scenarios. *Waste Biomass Valor.* **2012**, *3*, 249–257. [[CrossRef](#)]
6. Wei, L.L.; Zhao, Q.L.; Hu, K.; Lee, D.J.; Xie, C.M.; Jiang, J.Q. Extracellular biological organic matters in sewage sludge during mesophilic digestion at reduced hydraulic retention time. *Water Res.* **2011**, *45*, 1472–1480. [[CrossRef](#)]
7. Bakisgan, C.; Dumanli, A.G.; Yürüm, Y. Trace elements in Turkish biomass fuels: Ashes of wheat straw, olive bagasse and hazelnut shell. *Fuel* **2009**, *88*, 1842–1851. [[CrossRef](#)]
8. Hoşgün, E.Z.; Berikten, D.; Kıvanç, M.; Bozan, B. Ethanol production from hazelnut shells through enzymatic saccharification and fermentation by low-temperature alkali pretreatment. *Fuel* **2017**, *196*, 280–287. [[CrossRef](#)]
9. Haykiri-Acma, H.; Yaman, S.; Kucukbayrak, S. Combustion characteristics of sodium-free pyrolytic char from hazelnut shell. *Fuel Process. Technol.* **2012**, *96*, 169–174. [[CrossRef](#)]
10. Haykiri-Acma, H. The role of particle size in the non-isothermal pyrolysis of hazelnut shell. *J. Anal. Appl. Pyrolysis* **2006**, *75*, 211–216. [[CrossRef](#)]
11. Zhao, B.; Xu, X.; Xu, S.; Chen, X.; Li, H.; Zeng, F. Surface characteristics and potential ecological risk evaluation of heavy metals in the bio-char produced by co-pyrolysis from municipal sewage sludge and hazelnut shell with zinc chloride. *Bioresour. Technol.* **2017**, *243*, 375–383. [[CrossRef](#)]
12. Panepinto, D.; Tedesco, V.; Brizio, E.; Genon, G. Environmental Performances and Energy Efficiency for MSW Gasification Treatment. *Waste Biomass Valor.* **2014**, *6*, 123–135. [[CrossRef](#)]
13. Chen, D.; Yin, L.; Wang, H.; He, P. Pyrolysis technologies for municipal solid waste: A review. *Waste Manag.* **2014**, *34*, 2466–2486. [[CrossRef](#)] [[PubMed](#)]
14. Jin, J.; Li, Y.; Zhang, J.; Wu, S.; Cao, Y.; Liang, P.; Zhang, J.; Wong, M.H.; Wang, M.; Shan, S.; et al. Influence of pyrolysis temperature on properties and environmental safety of heavy metals in biochars derived from municipal sewage sludge. *J. Hazard. Mater.* **2016**, *320*, 417–426. [[CrossRef](#)] [[PubMed](#)]
15. Han, R.; Zhao, C.; Liu, J.; Chen, A.; Wang, H. Thermal characterization and syngas production from the pyrolysis of biophysical dried and traditional thermal dried sewage sludge. *Bioresour. Technol.* **2015**, *198*, 276–282. [[CrossRef](#)] [[PubMed](#)]
16. Zhao, B.; Xu, X.; Zeng, F.; Li, H.; Chen, X. The hierarchical porous structure bio-char assessments produced by co-pyrolysis of municipal sewage sludge and hazelnut shell and Cu(II) adsorption kinetics. *Environ. Sci. Pollut. Res.* **2018**, *25*, 19423–19435. [[CrossRef](#)]

17. Cao, Y.; Pawłowski, A. Sewage sludge-to-energy approaches based on anaerobic digestion and pyrolysis: Brief overview and energy efficiency assessment. *Renew. Sustain. Energy Rev.* **2012**, *16*, 1657–1665. [[CrossRef](#)]
18. Leng, L.; Yuan, X.; Huang, H.; Shao, J.; Wang, H.; Chen, X.; Zeng, G. Bio-char derived from sewage sludge by liquefaction: Characterization and application for dye adsorption. *Appl. Surf. Sci.* **2015**, *346*, 223–231. [[CrossRef](#)]
19. Leng, L.J.; Yuan, X.Z.; Huang, H.J.; Wang, H.; Wu, Z.B.; Fu, L.H.; Peng, X.; Chen, X.H.; Zeng, G.M. Characterization and application of bio-chars from liquefaction of microalgae, lignocellulosic biomass and sewage sludge. *Fuel Process. Technol.* **2015**, *129*, 8–14. [[CrossRef](#)]
20. Illera, V.; Walter, I.; Souza, P.; Cala, V. Short-term effects of biosolid and municipal solid waste applications on heavy metals distribution in a degraded soil under a semi-arid environment. *Sci. Total Environ.* **2000**, *255*, 29–44. [[CrossRef](#)]
21. Vardon, D.R.; Sharma, B.K.; Blazina, G.V.; Rajagopalan, K.; Strathmann, T.J. Thermochemical conversion of raw and defatted algal biomass via hydrothermal liquefaction and slow pyrolysis. *Bioresour. Technol.* **2012**, *109*, 178–187. [[CrossRef](#)]
22. Joan, J.M.; José, L.S.; Javier, Á.; Alberto, G.; Jesús, A. Influence of gas residence time and air ratio on the air gasification of dried sewage sludge in a bubbling fluidized bed. *Fuel* **2006**, *85*, 2027–2033. [[CrossRef](#)]
23. Petersen, I.; Werther, J. Three-dimensional modeling of a circulating fluidized bed gasifiers for sewage sludge. *Chem. Eng. Sci.* **2005**, *60*, 4469–4484. [[CrossRef](#)]
24. Bodo, G.; Christian, E.; Peter, G.; Juri, H.; Klaus, K. Energy recovery from sewage sludge by means of fluidized bed gasification. *Waste Manag.* **2008**, *28*, 1819–1826. [[CrossRef](#)]
25. Tran, H.N.; You, S.J.; Chao, H.P. Fast and efficient adsorption of methylene green 5 on activated carbon prepared from new chemical activation method. *J. Environ. Manag.* **2017**, *188*, 322–336. [[CrossRef](#)]
26. Okman, I.; Karagöz, S.; Tay, T.; Erdem, M. Activated carbons from grape seeds by chemical activation with potassium carbonate and potassium hydroxide. *Appl. Surf. Sci.* **2014**, *293*, 138–142. [[CrossRef](#)]
27. Dietl, T.; Ohno, H.; Matsukura, F.; Cibert, J.; Ferrand, D. Zener model description of ferromagnetism in zinc-blende magnetic semiconductors. *Science* **2000**, *287*, 1019–1022. [[CrossRef](#)]
28. Park, S.K.; Park, J.H.; Ko, K.Y.; Yoon, S.; Chu, K.S.; Kim, W.; Do, Y.R. Hydrothermal–electrochemical synthesis of ZnO nanorods. *Cryst. Growth Des.* **2009**, *9*, 3615–3620. [[CrossRef](#)]
29. Ruggieri, F.; D’Archivio, A.A.; Fanelli, M.; Santucci, S. Photocatalytic degradation of linuron in aqueous suspensions of TiO₂. *RSC Adv.* **2011**, *1*, 611–618. [[CrossRef](#)]
30. Zheng, R.; Liu, H.; Zhang, X.; Roy, V.; Djurišić, A. Exchange bias and the origin of magnetism in Mn-doped ZnO tetrapods. *Appl. Phys. Lett.* **2004**, *85*, 2589–2591. [[CrossRef](#)]
31. Xu, X.; Zhao, B.; Sun, M.; Chen, X.; Zhang, M.; Li, H.; Xu, S. Co-pyrolysis characteristics of municipal sewage sludge and hazelnut shell by TG-DTG-MS and residue analysis. *Waste Manag.* **2017**, *62*, 91–100. [[CrossRef](#)] [[PubMed](#)]
32. Agrafioti, E.; Bouras, G.; Kalderis, D.; Diamadopoulos, E. Biochar production by sewage sludge pyrolysis. *J. Anal. Appl. Pyrolysis* **2013**, *101*, 72–78. [[CrossRef](#)]
33. Hunsom, M.; Autthanit, C. Adsorptive purification of crude glycerol by sewage sludge-derived activated carbon prepared by chemical activation with H₃PO₄, K₂CO₃ and KOH. *Chem. Eng. J.* **2013**, *229*, 334–343. [[CrossRef](#)]
34. Zhao, B.; Xu, X.; Li, H.; Chen, X.; Zeng, F. Kinetics evaluation and thermal decomposition characteristics of co-pyrolysis of municipal sewage sludge and hazelnut shell. *Bioresour. Technol.* **2018**, *247*, 21–29. [[CrossRef](#)]
35. Sing, K.S.; Everett, D.H.; Haul, R.A.W.; Moscou, L.; Pierotti, R.A.; Rouquerol, J.; Siemieniewska, T. Reporting physisorption data for gas/solid systems with special reference to the determination of surface area and porosity. *Pure Appl. Chem.* **1985**, *57*, 603–619. [[CrossRef](#)]
36. Xue, G.; Gao, M.; Gu, Z.; Luo, Z.; Hu, Z. The removal of p-nitrophenol from aqueous solutions by adsorption using gemini surfactants modified montmorillonites. *Chem. Eng. J.* **2013**, *218*, 223–231. [[CrossRef](#)]
37. Wang, P.; Tang, L.; Wei, X.; Zeng, G.; Zhou, Y.; Deng, Y.; Wang, J.; Xie, Z.; Fang, W. Synthesis and application of iron and zinc doped biochar for removal of p-nitrophenol in wastewater and assessment of the influence of co-existed Pb(II). *Appl. Surf. Sci.* **2017**, *392*, 391–401. [[CrossRef](#)]
38. Zhang, F.S.; Nriagu, J.O.; Itoh, H. Mercury removal from water using activated carbons derived from organic sewage sludge. *Water Res.* **2005**, *39*, 389–395. [[CrossRef](#)]

39. Bogusz, A.; Nowak, K.; Stefaniuk, M.; Dobrowolski, R.; Oleszczuk, P. Synthesis of biochar from residues after biogas production with respect to cadmium and nickel removal from wastewater. *J. Environ. Manag.* **2017**, *201*, 268–276. [[CrossRef](#)]
40. Pelleri, F.M.; Giannis, A.; Kalderis, D.; Anastasiadou, K.; Stegmann, R.; Wang, J.-Y.; Gidakos, E. Adsorption of Cu(II) ions from aqueous solutions on biochars prepared from agricultural by-products. *J. Environ. Manag.* **2012**, *96*, 35–42. [[CrossRef](#)]
41. Cao, J.S.; Lin, J.X.; Fang, F.; Zhang, M.T.; Hu, Z.-R. A new absorbent by modifying walnut shell for the removal of anionic dye: Kinetic and thermodynamic studies. *Bioresour. Technol.* **2014**, *163*, 199–205. [[CrossRef](#)] [[PubMed](#)]
42. Li, M.; Liu, Q.; Guo, L.; Zhang, Y.; Lou, Z.; Wang, Y.; Qian, G. Cu(II) removal from aqueous solution by *Spartina alterniflora* derived biochar. *Bioresour. Technol.* **2013**, *141*, 83–88. [[CrossRef](#)] [[PubMed](#)]

Publisher's Note: MDPI stays neutral with regard to jurisdictional claims in published maps and institutional affiliations.



© 2020 by the authors. Licensee MDPI, Basel, Switzerland. This article is an open access article distributed under the terms and conditions of the Creative Commons Attribution (CC BY) license (<http://creativecommons.org/licenses/by/4.0/>).